

Special Issue:

Compound Semiconductors

Guest-Edited by Masaaki Tanaka,
Masakazu Sugiyama, Takuro Fujii,
and Shinobu Ohya



Molecular Beam Epitaxy of Transition Metal Nitrides for Superconducting Device Applications

D. Scott Katzer, Neeraj Nepal, Matthew T. Hardy, Brian P. Downey, David F. Storm, Eric N. Jin, Rusen Yan, Guru Khalsa, John Wright, Andrew C. Lang, Tyler A. Growden, Vikrant Gokhale, Virginia D. Wheeler, Alan R. Kramer, Joan E. Yater, Huili Grace Xing, Debdeep Jena, and David J. Meyer*

Epitaxial integration of superconductors with semiconductors is expected to enable new device architectures and to increase electronic circuit and system functionality and performance in diverse fields, including sensing and quantum computing. Herein, radiofrequency plasma molecular-beam epitaxy is used to epitaxially grow 3–200 nm-thick metallic NbN_x and TaN_x thin films on hexagonal SiC substrates. Single-phase cubic $\delta\text{-NbN}$ and hexagonal TaN_x films are obtained when the starting substrate temperature is ≈ 800 and ≈ 900 °C, respectively, and the active N to Nb or Ta ratio is $\approx 2.5\text{--}3$. The films are characterized using in-situ reflection high-energy electron diffraction and ex-situ atomic force microscopy, contactless sheet resistance, X-ray diffraction, X-ray photoelectron spectroscopy, secondary ion-mass spectrometry, Rutherford backscattering spectrometry, cross-sectional transmission electron microscopy, and low-temperature electrical measurements. Smooth, epitaxial, low-resistivity films of cubic $\delta\text{-NbN}$ and hexagonal TaN_x on SiC are demonstrated for films at least ≈ 50 nm-thick, and their superconducting properties are reported. Epitaxy of AlN and GaN on $\delta\text{-NbN}$ is also demonstrated, as well as integration of an epitaxial NbN_x superconducting electrode layer under GaN high-electron mobility transistors. These early demonstrations show the promise of direct epitaxial integration of superconducting transition metal nitrides with group III-N semiconductors.

1. Introduction

Although the advantages of epitaxial metal layers in devices such as metal-base transistors, including low base resistance and small base transit time, were predicted as early as the 1960s,^[1] the successful realization of high-quality epitaxial metals on semiconductors, and semiconductors on metals, has remained elusive. Sands et al. reviewed the progress and status of research on epitaxial metals on III–V compounds in 1990.^[2] More recently, researchers have investigated ZrB_2 ^[3–5] and TiC ^[6,7] metallic substrates for GaN heteroepitaxial growth and device fabrication, and superconducting cubic niobium nitride (NbN_x) has been grown on GaN and AlGaN by sputtering.^[8,9]


NbN_x and tantalum nitride (TaN_x) are transition metal nitrides (TMNs) (also called “interstitial nitrides”) with many compelling properties.^[10] TMNs such as NbN_x have been studied for decades and have many practical applications due to their mechanical, chemical, and electrical

properties.^[11] The cubic $\delta\text{-NbN}$ crystalline phase of NbN_x is a well-known superconductor which has been used for superconducting

Dr. D. S. Katzer, Dr. N. Nepal, Dr. M. T. Hardy, Dr. B. P. Downey, Dr. D. F. Storm, Dr. V. D. Wheeler, Dr. J. E. Yater, Dr. D. J. Meyer
Electronics Science and Technology Division
U. S. Naval Research Laboratory
4555 Overlook Avenue, S.W., Washington, DC 20375-5347, USA
E-mail: scott.katzer@nrl.navy.mil

Dr. E. N. Jin, Dr. T. A. Growden, Dr. V. Gokhale, Dr. A. R. Kramer
NRC Research Associateships Programs
500 Fifth Street, Washington, DC 20001, USA

Dr. R. Yan, Dr. H. G. Xing, Dr. D. Jena
School of Electrical and Computer Engineering
Cornell University
Ithaca, NY 14853, USA

 The ORCID identification number(s) for the author(s) of this article can be found under <https://doi.org/10.1002/pssa.201900675>.

DOI: 10.1002/pssa.201900675

Dr. G. Khalsa, J. Wright, Dr. H. G. Xing, Dr. D. Jena
Department of Materials Science and Engineering
Cornell University
Ithaca, NY 14853, USA

Dr. G. Khalsa
School of Applied and Engineering Physics
Cornell University
Ithaca, NY 14853, USA

Dr. A. C. Lang
American Society for Engineering Education
Projects Office
1818 N. Street, Suite 600, Washington, DC 20036, USA

Dr. H. G. Xing
Kavli Institute at Cornell for Nanoscale Science
Cornell University
Ithaca, NY 14853, USA

radiofrequency circuits,^[12] squid magnetometers,^[13] Josephson junctions,^[14] and single-photon detectors^[15] for quantum communications and astronomy, and a variety of other applications.^[16] Less well-known, hexagonal β -Nb₂N is another one of the several stable phases of niobium–nitrogen compounds that is of particular interest for epitaxial growth. Hexagonal β -Nb₂N and the corresponding hexagonal phase γ -Ta₂N are members of the P₆₃/mmc space group with the lattice parameters $a = 0.3056$ nm and $c = 0.4995$ nm for Nb₂N and $a = 0.30476$ nm and $c = 0.49187$ nm for Ta₂N.^[17] As shown in the VESTA ball-and-stick crystal models in **Figure 1a,b**,^[18] these hexagonal phases have a near-lattice-matched hexagonal structure that is similar but not identical to the hexagonal structure of 6H-SiC (P₆₃mc, $a = 0.3081$ nm, $c = 1.510$ nm).^[19] Hexagonal SiC substrates are technologically important for the heteroepitaxial growth of high-performance III–N materials due to their high thermal conductivity. Figure 1c shows that the [111]-oriented cubic δ -NbN crystalline phase with space group Fm $\bar{3}$ m and $a = 0.446$ nm (pseudo-hexagonal $a = 0.446$ nm / $\sqrt{2} = 0.315$ nm) also has close atomic registry to SiC. There is still some controversy about the crystalline phases of TaN_x compounds, with the hexagonal δ -TaN phase having been variously identified as the WC-like phase (P $\bar{6}$ m2), P₆₃/mmc,^[17] and wurtzite (P₆₃mc).^[20] Note that the N-site occupancy is ideally 0.5 for the Nb₂N and Ta₂N hexagonal phases, whereas it is ideally 1.0 for the cubic NbN phase and the hexagonal TaN phase. Other TMNs that could be considered for epitaxial integration with SiC and III–N semiconductors include TiN, ZrN, HfN, VN, MoN, and WN.^[21]

The wide bandgap group III nitride semiconductors are also members of the P₆₃mc space group like SiC. They have shown promise in a variety of modern electronics systems including ultrafast microwave communications,^[22] ultralow-power computation,^[23] high-voltage switches,^[24] infrared through visible- to deep-ultraviolet photonic emitters and detectors,^[25,26] and high-frequency circuit components such as surface acoustic wave and bulk acoustic wave filters.^[27] Substantial advances in electronic systems would be expected if the electronic functionality of group III–N semiconductors could be combined with that of superconductors on a single epitaxial platform.^[28–31] Integration of 2D superconducting gallium layers has been reported recently on GaN and other substrates.^[32–34]

D. Scott Katzer obtained his A.B. degree in Physics from the University of Chicago in 1983. His Ph.D. degree in Solid-State Electronics was awarded by the University of Cincinnati in 1988. His dissertation was on GaAs CCD imagers under the direction of Prof. Peter B. Kosel. Since 1989, he has been with the U.S. Naval Research Laboratory performing MBE-based research on III–V, III–N, and TMN materials, as well as ultra-wide bandgap semiconductors including Ga₂O₃.

Little has been reported on the epitaxy of hexagonal phases of TMNs on hexagonal substrates for integration with III–N semiconductor devices to date. The promise of achieving a near-lattice-matched hexagonal metal to hexagonal III–N materials by changing only the cation from Ga or Al to Nb or Ta makes Nb₂N and Ta₂N, and hexagonal TaN, especially intriguing for use in III–N epitaxy compared with TiC^[3–5] or ZrB₂^[6,7] where both the cation and anion change across the interface. There has also been little reported on the superconducting properties of the hexagonal phases, other than they are known to either not be superconducting or to have much lower transition temperatures than the cubic phase.

Here, we review progress in the epitaxial growth of NbN_x and TaN_x on SiC using molecular beam epitaxy (MBE), discuss the properties of the materials, and demonstrate successful epitaxial integration of the semiconducting III–N and superconducting TMN materials families as a crucial enabler for future superconducting device applications.

2. MBE of TMNs on SiC

In this section, the system used for the MBE growth of TMNs on hexagonal 4H- and 6H-SiC substrates is discussed along with its important features. The use of equilibrium phase diagrams to understand and reduce the growth space investigated, and thereby more rapidly climb the growth learning curve, is also described. Finally, the growth conditions used to grow NbN_x and TaN_x TMNs epitaxially on SiC are described.

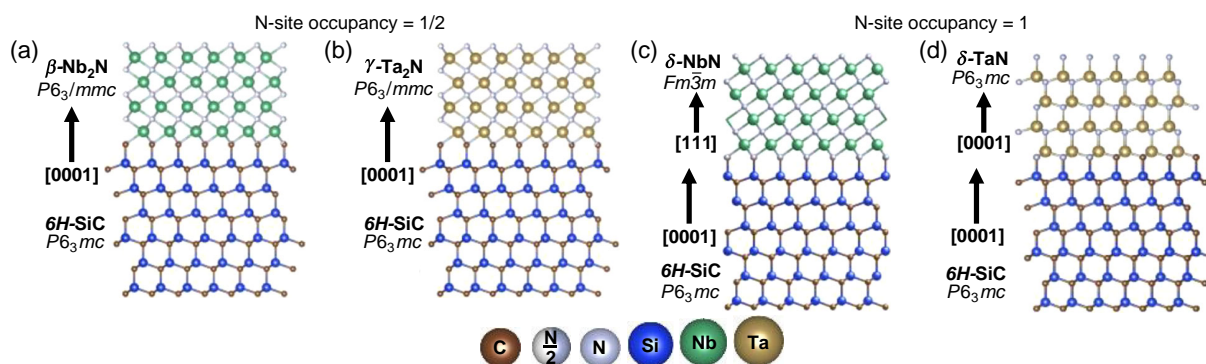


Figure 1. Ball-and-stick crystal models of the epitaxial TMNs on SiC considered here. a) hexagonal β -Nb₂N, b) hexagonal γ -Ta₂N, c) [111]-oriented cubic δ -NbN_x, and d) hexagonal (wurtzite) δ -TaN_x. Note that the ideal N-site occupancy is 0.5 for the hexagonal Nb₂N and Ta₂N phases and 1.0 for the cubic NbN_x and the hexagonal TaN_x phases.

2.1. MBE Growth System

The epitaxial growth was performed in a customized Scienta-Omicron PRO-75 MBE growth chamber with liquid-nitrogen cooled cryopanel having a base pressure below 2×10^{-11} Torr, as described previously.^[35,36] Niobium and tantalum have extremely low vapor pressures below the 2000 °C maximum temperature limit of conventional effusion cells, so electron beam (e-beam) evaporation is the only practical method to evaporate these elements in a UHV system. The niobium flux, f_{Nb} , and tantalum flux, f_{Ta} , were generated by an in-situ 5 kW e-beam evaporator. The elemental niobium or tantalum source material was 99.95% pure Nb (excluding Ta at 90 ppmw) or Ta pellets (Nb at 26 ppmw), with the principal impurities being O, C, W, and N loaded in a W hearth liner. The incident reactive nitrogen flux, f_{N} , was generated by a Veeco Uni-Bulb RF-plasma source using a 99.9999% pure N₂ gas that was further purified using an inline purifier. The flux from a Uni-Bulb RF-plasma source is typically found to be a mixture of atoms, ions, and excited molecules^[37] but was not characterized further in this study.

Reflection high-energy electron diffraction (RHEED) was performed in-situ in the PRO-75 using a Staib Instruments RH20 RHEED system operated at 13.5 keV accelerating voltage and 1–2 μA beam current. The e-beam evaporator electromagnets caused a ≈ 1 cm lateral shift in the RHEED pattern when the e-beam was at high voltage, but they did not otherwise significantly disturb the RHEED images.

2.2. MBE Growth Conditions for TMNs and Heterostructures

Figure 2 shows the equilibrium phase diagrams for a) Nb–N compounds and b) Ta–N compounds.^[38] Although MBE is in general not an equilibrium growth process, the phase diagrams can allow us to make inferences about the expected growth conditions necessary to obtain single-phase materials and to be aware of potential complications. For example, the Nb–N phase diagram indicates that at atmospheric pressure a minimum

temperature of around 780 °C is needed for the formation of the hexagonal β -Nb₂N phase, whereas temperatures above 1200 °C are needed to form the so-called “high-temperature” phase cubic δ -NbN_x. Another important detail to note is that the β -Nb₂N and δ -NbN_x crystalline phases exist over a fairly wide composition range, and in fact both crystalline phases can exist in certain composition ranges (N-rich β -Nb₂N and N-lean δ -NbN_x). For the case of Ta–N, the shape of the phase diagram is similar, but the hexagonal δ -Ta_xN phase is well separated on the composition axis from the hexagonal γ -Ta₂N phase. Therefore, we might expect that the hexagonal Ta₂N or TaN phase purity would be easier to control compared with the niobium case. Since these equilibrium phase diagrams are very similar (except that higher minimum temperatures are generally required for Ta_xN phase formation), one could expect to be able to transfer NbN_x MBE growth knowledge to epitaxial Ta_xN by using similar flux conditions and simply increasing the Ta_xN growth temperature above that used for NbN_x. We investigated the growth parameter space of NbN_x and found this to be the case. In particular, the MBE growth window for single-phase Ta_xN seems to require substrate temperatures greater than ≈ 900 °C to obtain single-phase epitaxial material on SiC when using N-rich MBE growth conditions, whereas temperatures above ≈ 775 °C are required for single-phase NbN_x, as discussed below.^[39,40]

Since the stable NbN_x and Ta_xN films exist over a range of compositions and exhibit multiple crystal structures, the niobium-based TMN films will be referred to hereafter as “NbN_x” and the tantalum-based TMN films will be referred to as “Ta_xN” unless we are specifically addressing their crystalline phase. We will also use “TMN” below to refer to either NbN_x or Ta_xN (but not other TMN compounds).

TMN thin films were grown on 3-in.-diameter [0001]-oriented semi-insulating (SI) Si-face 6H- or 4H-SiC substrates that had been chemically–mechanically polished to an epi-ready finish. No ex-situ cleaning or backside metallization of the substrates was performed in this study. After the SiC substrate was thermally cleaned in the MBE growth chamber at temperatures of

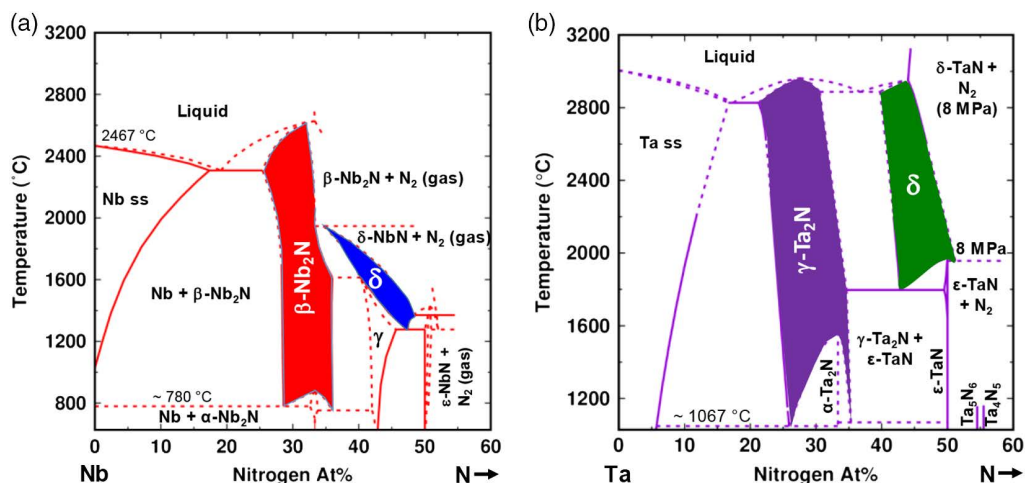


Figure 2. Equilibrium phase diagram for a) niobium and nitrogen, and b) tantalum and nitrogen. Note that both TMN systems are quite complex, but they are qualitatively similar for the hexagonal phases of interest except for the higher temperatures required for phase formation in the tantalum-nitrogen case. The hexagonal β -Nb₂N, cubic δ -NbN_x, hexagonal γ -Ta₂N, and hexagonal δ -Ta_xN phases of interest are highlighted. Reproduced with permission.^[40] Copyright 2019, American Institute of Physics.

≈800–900 °C for 10 min, the substrate temperature was changed to the desired fixed value and allowed to stabilize. To date, in experiments using nitrogen-rich growth conditions, the substrate temperature is the most important growth parameter controlling the TMN metallic film growth on SiC. It should be noted that the real temperature of radiatively heated substrates can increase dramatically as a result of increased IR absorption during the MBE growth of semiconductors with bandgaps smaller than the substrate.^[41] The deposition of zero-bandgap metals on a wide-bandgap substrate would also lead to more reflection of IR radiation back toward the substrate heater thermocouple as the thickness increased. Thus, the evolution of the TMN/SiC surface temperature may be expected to be a strong function of the TMN thickness and deposition conditions. For simplicity, all of the growth temperatures discussed here were the starting temperatures of the SiC substrate, estimated by scaling the substrate heater thermocouple temperature which was calibrated via excess Ga surface coverage measurements during GaN growth.^[42]

While the substrate temperature was stabilizing, the e-beam source was set to operating conditions to achieve the desired f_{Nb} or f_{Ta} , and the N^* plasma was started. The TMN deposition rate was principally determined by the f_{Nb} or f_{Ta} and was typically 1.2 nm min^{-1} ($\approx 1.1 \times 10^{14} \text{ cm}^{-2} \text{ s}^{-1}$), as measured using a quartz crystal microbalance (QCM). The RF-plasma power levels were ≈25 W higher than the minimum required for a stable “high-brightness” plasma (i.e., 250–370 W depending on the age of the source’s plasma chamber), and the N_2 flow rate was in the range of 0.8–1.2 sccm. The chamber pressure during growth was $1\text{--}2 \times 10^{-5}$ Torr. The resultant f_{N^*} was nominally $\approx 3.3 \text{ nm min}^{-1}$ as determined from measured N-limited GaN growth rates. Note that the implicit simplifying assumption that f_{N^*} incorporates in TMN the same way as it does in GaN is unlikely to hold because TMNs can form without excited nitrogen. However, relating the f_{N^*} to an equivalent N-limited GaN growth rate is a helpful metric for comparison to conventional III-N MBE growth conditions. After a 10 min plasma stabilization delay, the TMN growth was initiated by opening the N^* , e-beam, and substrate shutters sequentially, and the growth continued until the desired thickness was reached.

In samples where III-N heterostructures were grown in situ immediately after the TMN growth was completed, the e-beam evaporator was returned to a low-power state, the substrate temperature and N^* fluxes were adjusted to the values needed for III-N epitaxy, and the III-N growth was then started in the usual way as if the growth were being performed directly on SiC.

3. Characterization of TMNs and III-N/TMN Heterostructures

In this section, the various characterization methods used to determine the properties of the TMN films are described along with the results obtained. Section 3.1 discusses in-situ RHEED. Section 3.2 is the first of several sections on ex-situ measurements and includes atomic force microscopy (AFM). Section 3.3 describes contactless sheet resistance measurements and results. Section 3.4 gives an overview of X-ray diffraction (XRD) measurements. Selected samples were characterized by methods discussed in Section 3.5 to directly extract chemical composition

information—X-ray photoelectron spectroscopy (XPS), Rutherford backscattering spectrometry (RBS), and secondary ion mass spectroscopy (SIMS). Section 3.6 discusses transmission electron microscopy (TEM) results obtained on selected samples. Finally, Section 3.7 presents electronic and superconducting properties of several MBE-grown TMN structures.

3.1. Reflection High-Energy Electron Diffraction (RHEED)

When the MBE growth conditions for the TMN films are correctly optimized, the RHEED pattern changes smoothly at the initiation of film growth without the appearance of island-induced roughness on the Si-face hexagonal SiC substrate. Moreover, the streaky RHEED pattern is maintained throughout the remainder of the TMN film growth. **Figure 3a** shows the post-growth RHEED pattern observed on a 20-nm-thick NbN_x film grown on 6H-SiC. A clear, bright, 2×2 reconstruction was present on this surface. **Figure 3b** shows the post-growth RHEED pattern observed on a 43-nm-thick TaN_x film grown on 6H-SiC. A clear, bright, 3×1 reconstruction was present on this surface. Wang et al. reports that a 2×2 reconstruction is a signature of N-lean NbN_x epitaxy,^[43] whereas **Figure 3b** is the first known report of a surface reconstruction on TaN_x . All of the high-quality NbN_x and TaN_x films grown on hexagonal SiC by MBE have had a sixfold in-plane rotational symmetry in RHEED. Smoother TMN films generally correlated with smooth, streaky RHEED patterns.

As in other material systems, RHEED can be used for optimizing the growth conditions (especially the growth temperature) of the TMN films grown on SiC. In general, spottiness in the RHEED pattern, especially in the first 5–10 nm of growth, is usually an indication that the substrate temperature is too low. In contrast, rapid dimming of the RHEED pattern can be an indication that the epitaxy is degrading and the surface is rapidly roughening, which may indicate that excessive nitrogen is being lost from the film because the substrate temperature is too high for the f_{N^*} used.

3.2. Atomic Force Microscopy (AFM)

TMN samples were characterized by AFM using a Bruker Fast Scan system operated in tapping mode. **Figure 4a** shows a $1 \times 1 \mu\text{m}^2$ AFM image of the surface of a 20-nm-thick NbN_x epitaxial film having a root mean square (rms) roughness of 0.46 nm.^[39] The rms roughness often increases with NbN_x thickness, but the surface is still smooth (i.e., rms < 0.5 nm) for films at least 200 nm thick if the growth conditions are optimized. For very thin films with thicknesses below 10 nm, the surface roughness is basically unchanged from the roughness of the epi-ready SiC substrate (rms roughness as low as ≈0.1 nm), and the NbN_x film retains the atomic step morphology of the underlying SiC.

Figure 4b shows representative post-growth $10 \times 10 \mu\text{m}^2$, $3 \times 3 \mu\text{m}^2$, and $1 \times 1 \mu\text{m}^2$ AFM scans of the same 43-nm-thick TaN_x film shown in **Figure 3b**.^[40] The film is smooth over all three length scales with rms roughnesses less than 0.5 nm in each case (as indicated by the numbers inset in the images). The $3 \times 3 \mu\text{m}^2$ scan shows faint, nearly parallel lines that are surface steps mimicking those in the starting SiC surface.

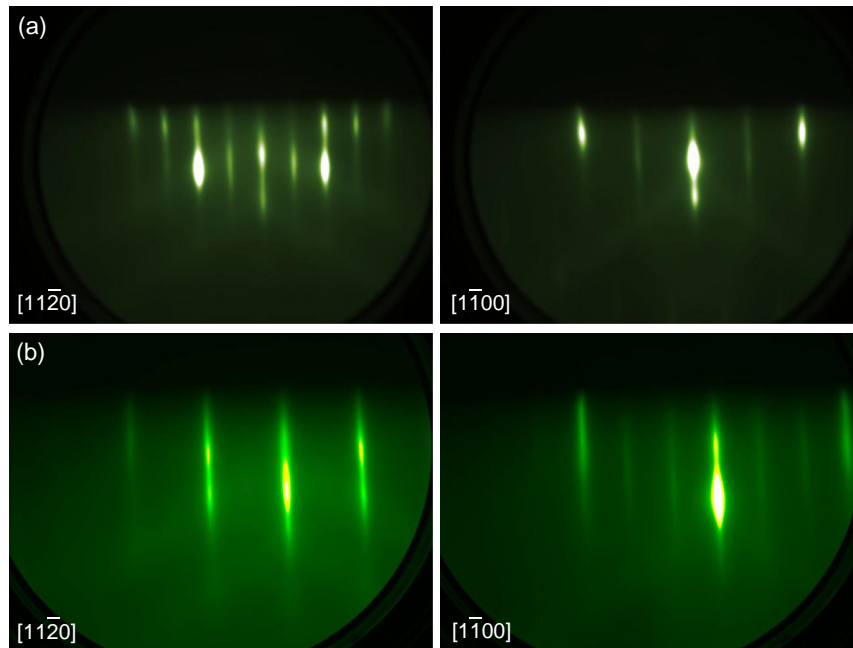


Figure 3. a) Post-growth RHEED patterns for 20-nm-thick NbN_x film grown on 6H-SiC. Note the clear, bright, 2×2 reconstruction. Reproduced with permission.^[39] Copyright 2015, IOP Publishing. b) Post-growth RHEED pattern for 43-nm-thick TaN_x film grown on 6H-SiC. Note the clear, bright, 1×3 reconstruction. Reproduced with permission.^[40] Copyright 2019, American Institute of Physics.

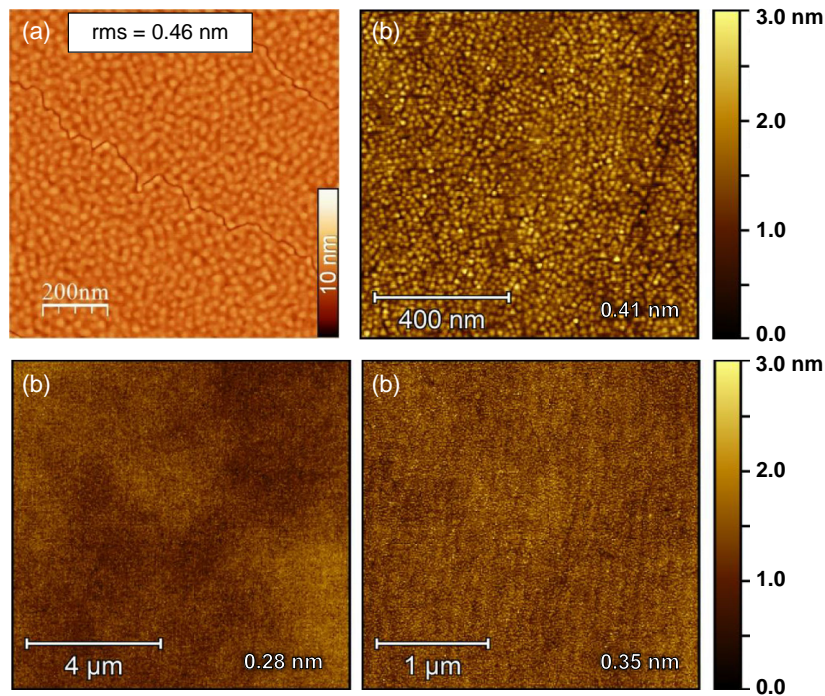


Figure 4. a) Post-growth AFM image for 20-nm-thick NbN_x film grown on 6H-SiC. The rms roughness is 0.46 nm. Note that the film reproduces the step-edges of the starting SiC substrate. Reproduced with permission.^[39] Copyright 2015, IOP Publishing. b) Post-growth AFM images for 43-nm-thick TaN_x film grown on 6H-SiC. The film is very smooth, having rms roughness < 0.5 nm for all scan ranges between $10 \times 10 \mu\text{m}^2$ and $1 \times 1 \mu\text{m}^2$. Reproduced with permission.^[40] Copyright 2019, American Institute of Physics.

The $1 \times 1 \mu\text{m}^2$ image shows a fine surface grain structure without any obvious orientation dependence. No attempt was made to deconvolute the tip geometry in the $1 \times 1 \mu\text{m}^2$ scan.^[44]

In general, smooth epitaxial TMN films can be grown by MBE on SiC and the surface morphology is similar for NbN_x and TaN_x films.

3.3. Contactless Sheet Resistance Measurements

Contactless sheet resistance measurements of the TMN films were performed with a Lehightronics 1510B system. Figure 5a shows a summary of room temperature contactless resistivity measurements^[45] of several NbN_x and TaN_x films grown at 800 and 900 °C, respectively, with differing thicknesses.^[39,40] The sheet resistance measurements were taken on a 55-point grid covering the 3-in.-diameter substrate (with 0.1-in. edge exclusion). The resistivity values shown in Figure 5a are the minimum measured values. Excellent resistivity uniformity was obtained on many samples: for example, a 10-nm-thick NbN_x sample had a uniformity value (defined as standard deviation divided by the mean) of 2.2%. The minimum NbN_x resistivity measured was $40 \mu\Omega \text{ cm}$ for a 100-nm-thick sample grown at 800 °C. This is substantially lower than the $\approx 80\text{--}90 \mu\Omega \text{ cm}$ resistivity reported for 1- μm -thick sputtered NbN_x films on Si substrates.^[46] As the thickness decreases from 100 to 30 nm, the film resistivity remains approximately constant at $40 \mu\Omega \text{ cm}$. For thicknesses below 30 nm, the resistivity increases rapidly as the film thickness decreases, likely due to increased carrier scattering by the interfaces.^[47]

The minimum resistivity of a 43-nm-thick TaN_x sample was $66 \mu\Omega \text{ cm}$. As expected, the resistivity trend with TaN_x thickness is similar to the case for NbN_x , with the points shifted up due to the higher resistivity of tantalum compared with niobium. However, to date, the resistivity of very thin TaN_x films is substantially higher than that of comparable-thickness NbN_x films.

These measurements have not been corrected to account for the formation of few-nm-thick NbO_x and TaO_x native surface oxides, which may be important when characterizing the resistivity of very thin air-exposed films. The thickest TaN_x film

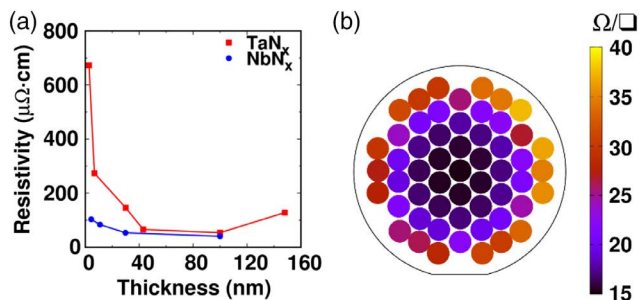


Figure 5. a) Post-growth contactless sheet resistance measurements for MBE-grown NbN_x/SiC and TaN_x/SiC giving resistivity as a function of film thickness. Minimum NbN_x resistivity is $40 \mu\Omega \text{ cm}$, whereas that for TaN_x is $66 \mu\Omega \text{ cm}$. b) Contactless sheet resistance measurements across a 43-nm-thick TaN_x film grown on a 3-in. diameter SiC wafer. Reproduced with permission.^[40] Copyright 2019, American Institute of Physics.

resistivity is higher than the trend value, likely due to the need for more growth optimization for very thick films.

Figure 5b shows the contactless sheet resistance measured at 55 points across the 3-in.-diameter 43-nm-thick $\text{TaN}_x/\text{6H-SiC}$ sample grown at 900 °C. The lowest sheet resistance is in the center, as is typical for most MBE-grown TMN films. The sheet resistance nonuniformity across the wafer is 28.8%. The relatively high nonuniformity is expected to be reduced with further optimization of the TMN MBE growth process.

3.4. X-ray Diffraction (XRD)

XRD measurements were performed using a 9 kW Rigaku SmartLab system equipped with a rotating copper anode. Figure 6 shows a summary of the XRD results for 100-nm-thick NbN_x films grown by MBE on SiC at several fixed substrate temperatures for similar Nb and N* fluxes.^[39] Measurements from the sample grown at 675 °C show weak diffraction peaks at angles corresponding to the reported peak positions for: the metastable hexagonal δ' phase with $x \sim 0.97$, the ϵ phase with $x \sim 1.01$, and the cubic δ phase with $x \sim 1.0$. This sample is a good example of how certain TMN growth conditions can lead to multiple crystalline phases coexisting in a single film. Increasing the growth temperature to 750 °C leads to the

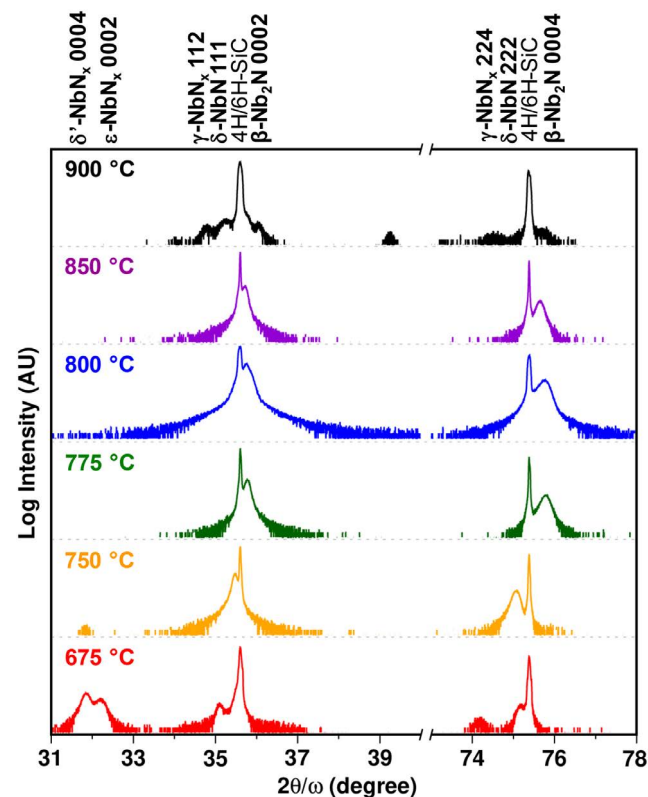


Figure 6. Symmetric XRD measurements of 100-nm-thick NbN_x/SiC structures as a function of growth temperature. The approximate expected positions of various reflection peaks are indicated at the top of the graph. Between about 775 and 850 °C, the NbN_x films are single-phase and appear to be predominantly cubic δ - NbN_x , but note the caveats in the main text. Reproduced with permission.^[39] Copyright 2015, IOP Publishing.

δ -NbN_x peak shifting to larger angles and the appearance of the tetragonal γ phase with $x \sim 0.80$, consistent with less N incorporation in the film. Increasing the substrate temperature further leads to the appearance of a peak to the right of the SiC peak that is consistent with the hexagonal β -Nb₂N phase.^[17] This change in phase behavior with increasing temperature is similar to previous reports on pulsed-laser or sputter-deposited NbN_x materials, wherein the phase obtained can be a strong function of the growth temperature (at least in the cases when the Nb and N* fluxes are not carefully matched),^[48,49] Single-phase NbN_x—either [111]-oriented cubic δ -NbN_x or [0001]-oriented hexagonal β -Nb₂N—is obtained at growth temperatures between 775 and 850 °C for these flux conditions. At 900 °C, the higher-angle NbN_x peak diminishes significantly and trace evidence of another lower-angle NbN_x phase begins to appear, indicating a loss of phase purity.

3.5. Chemical Composition by XPS/RBS/SIMS

The chemistry of TMNs is quite rich and complex compared with most semiconductors, so it is important to be able to quantify the chemical composition of the epitaxial TMN films. Also, while symmetric XRD measurements are commonly used for crystalline phase determination, it is important to recall that the NbN_x and TaN_x lattice constants vary with nitrogen content. In addition, the potential exists for lattice and thermal mismatches to introduce strains in the heteroepitaxial film. As a result of these factors, the XRD peak positions can vary from film to film without concurrent changes in crystalline phase.^[50] We have applied a variety of techniques to selected TMN films to quantify the composition and bonding in the films and to correlate those findings with XRD measurements.

Ex-situ XPS measurements were made either with a Thermo Scientific K-Alpha system^[39] or with an XPS system from StaiB Instruments.^[51] Representative data are shown in **Figure 7** for a 100 nm-thick NbN_x film.^[39] Figure 7 shows the measured Nb 3d and N 1s XPS spectra taken after 1 keV low-current Ar-sputter cleaning of the air-exposed surface. The deconvoluted N 1s spectrum shown in the lower graph still shows evidence of oxygen contamination, so the sputter cleaning was insufficient to completely remove the native oxide. In addition, ex-situ XPS Ar-sputter cleaning can preferentially etch N compared with Nb atoms, changing the measured N/Nb ratio. Recognizing these nonidealities in the measurements, the binding energy of the single Nb 3d 5/2 peak shown in the upper graph is located at 202.8 eV, which lies between the previously reported values for δ -NbN (203.5–203.8 eV) and Nb metal (202.2 eV).^[52] In addition, the difference between the binding energies of the Nb 3d and N 1s peak is 194.5 eV, consistent with previous reports for Nb₂N films.^[49] Analyzing the total Nb 3d area relative to the total N 1s area obtained using standard techniques gives a Nb/N atomic ratio of 1.8 ($x = 1/1.8 = 0.56$).

Similar ex-situ XPS measurements of the 43-nm-thick TaN_x / 6H-SiC film after Ar-sputter cleaning (not shown) give a Ta content of 61–63 atomic percent (at%) (depending on the etch conditions) and a TaN_x atomic ratio x -value of 0.59–0.64, indicating that this is an N-rich hexagonal γ -Ta₂N film or an N-lean hexagonal δ -TaN film.

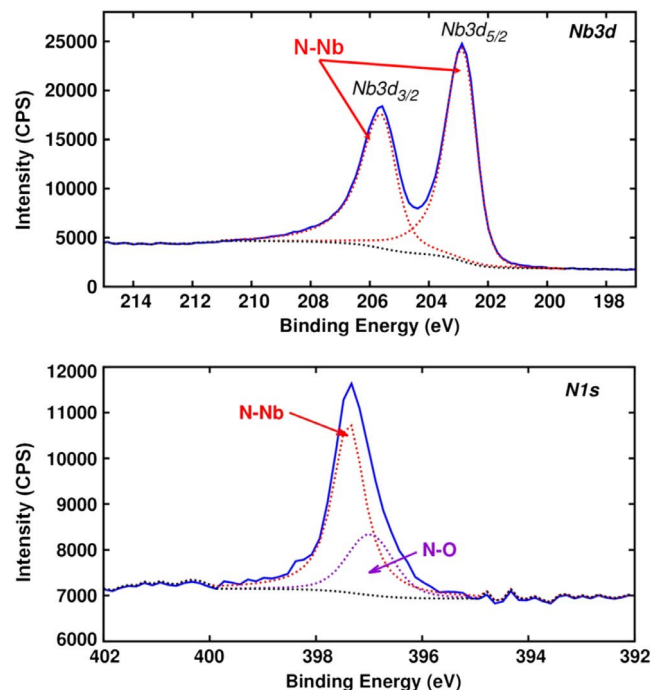


Figure 7. Ex-situ XPS measurements of a 100-nm-thick NbN_x film after low-energy sputter cleaning. Reproduced with permission.^[39] Copyright 2015, IOP Publishing.

Selected TMN films were also characterized by RBS and SIMS (not shown). In general, the films were uniform with less than 1 at% contamination by Nb in Ta and Ta in Nb. The Nb and Ta cross contamination was likely principally from the source materials used in the e-beam evaporator. The TMN films grown using the growth conditions described earlier and characterized to date have been N-lean cubic δ -NbN_x and N-rich hexagonal γ -Ta₂N (or N-lean hexagonal δ -TaN), consistent with the XRD and XPS results.

3.6. Cross-sectional Transmission Electron Microscopy (XTEM)

High-quality XTEM measurements of representative samples are an invaluable tool for the identification and verification of hexagonal β -Nb₂N, γ -Ta₂N, or δ -TaN epitaxial phases. For the NbN_x case, the complexity of the Nb–N phase diagram and the fact that several stable phases can coexist (some with overlapping compositions) can make phase identification difficult unless XTEM measurements are available. For the TaN_x case, there is in addition a lack of reported data on the epitaxy of this material to serve as a reference for comparison.

Figure 8 shows the a) XTEM measurements and b) symmetric XRD measurements of an NbN_x sample intentionally grown with a high Nb/N* ratio (Nb ~ 2.4 nm s⁻¹, N* ~ 1.8 nm s⁻¹). As shown by the red overlaid squares, at least two phases are present. By comparing the atomic stacking sequences between the XTEM image and the ball-and-stick models, and examining the 2D fast Fourier transforms (FFTs) of the selected areas in the image, the grains can be identified as (1) [0001]-oriented hexagonal β -Nb₂N (2) [111]-oriented cubic δ -NbN_x and (3) tentatively identified

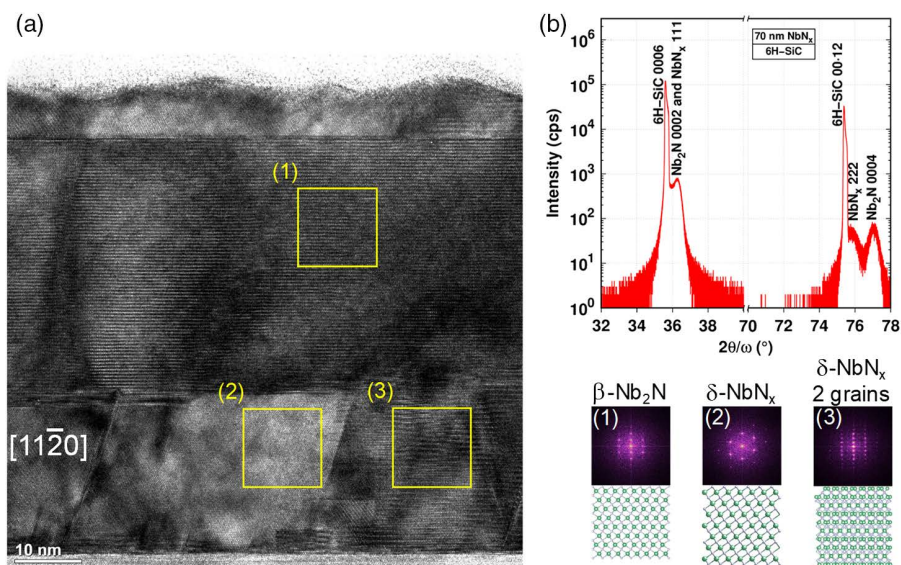


Figure 8. Cross-sectional transmission electron micrograph and XRD characterization of an NbN_x film grown with high Nb/N* flux ratio. The yellow square regions are where 2D FFT analysis is performed to determine the crystalline phase. The film shows multiple phases and in particular shows at least two crystalline phases are present. Region 1 is characteristic of most of the film and is identified as hexagonal $\beta\text{-Nb}_2\text{N}$. Region 2 is characteristic of a large fraction of the film, including near the SiC interface and in a rough surface layer, and is identified as cubic $\delta\text{-NbN}_x$. Region 3 is characteristic of isolated regions in the film and appears to be overlapping cubic [111]-oriented $\delta\text{-NbN}_x$ grains that are rotated modulo- 60° about the c-axis with respect to each other. Note that the peak to the right of the 6H-SiC 0006 peak cannot be fully resolved, but the second-order peak around the SiC 00-12 peak clearly shows two peaks corresponding to $\delta\text{-NbN}_x$ and $\beta\text{-Nb}_2\text{N}$.

overlapping [111]-oriented cubic $\delta\text{-NbN}_x$ grains with a modulo- 60° in-plane rotation between them. Comparison of the XTEM image with the XRD measurements (and published data) allows us to identify the right-most TMN peak at $\approx 77^\circ$ in Figure 8b as corresponding to the 0004 reflection of hexagonal $\beta\text{-Nb}_2\text{N}$; and the peak just to its left at $\approx 75.8^\circ$ as corresponding to the 222 reflection of cubic $\delta\text{-NbN}_x$. Note that the first-order NbN_x XRD peaks at $\approx 36.25^\circ$ are not separately resolved, so for this film it was important to extend the XRD measurement out to higher 2θ angles to access 2nd order peaks and increase their separation. Finally, in the XTEM image, note the sharp transition between the top hexagonal $\beta\text{-Nb}_2\text{N}$ interface and the bottom of the [111]-oriented cubic $\delta\text{-NbN}_x$ layer at the surface. The cause of the phase

change near the surface of the NbN_x film is not yet clear and is under investigation.

Figure 9a shows a representative XTEM micrograph of the 43-nm-thick TaN_x/SiC sample.^[40] The TaN_x film is uniform and single-phase except for isolated in-plane defects, and there is a sharp interface between the TaN_x film and the SiC substrate. A selected-area FFT (the gold square of the left image) yields a rectangular grid pattern of spots for this imaging orientation, indicating the TaN_x is hexagonal-symmetry crystalline material.^[53] **Figure 9b** shows an enlargement of the image on the left with CrystalMaker^[54] ball-and-stick models of hexagonal $\gamma\text{-Ta}_2\text{N}$ and wurtzite $\delta\text{-TaN}$ showing consistency between the image and either of the models. To date, using the N-rich

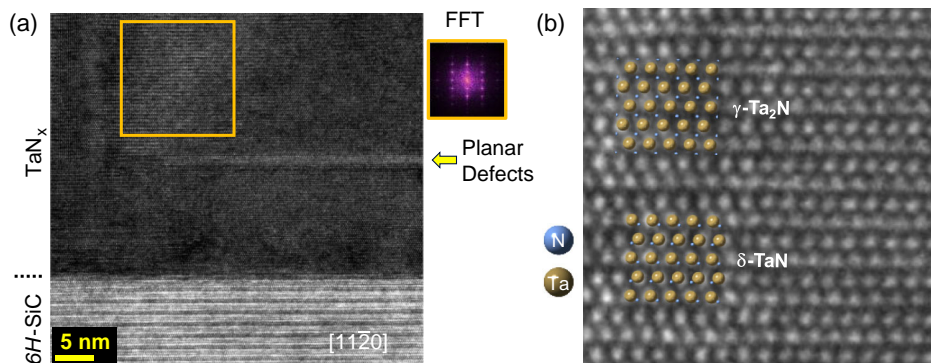


Figure 9. a) Cross-sectional transmission electron micrograph of 43-nm-thick TaN_x film on 6H-SiC. Isolated in-plane defects are present, but otherwise the TaN_x film appears to be uniform and single-phase. The selected area 2D FFT analysis indicates that the film is hexagonal. b) Enlargement of the boxed region shows the columns of Ta atoms in the image. Ball-and-stick models of hexagonal $\gamma\text{-Ta}_2\text{N}$ and wurtzite $\delta\text{-TaN}$ overlay the image and shows excellent agreement for both models, indicating the hexagonal phase is not uniquely determined yet. Reproduced with permission.^[40] Copyright 2019, American Institute of Physics.

growth conditions described earlier, a hexagonal TaN_x phase has been dominant in our MBE-grown TaN_x films, but identification of the particular hexagonal phase in this film is still in progress.

3.7. Electronic and Superconducting Properties of MBE-Grown TMNs

Cubic $\delta\text{-NbN}_x$ is a well-known superconductor with superconducting transition temperatures (T_c) as high as ≈ 17 K. The T_c for $\delta\text{-NbN}_x$ varies with the material quality and with the N/Nb atomic ratio “ x ”, with higher T_c generally being found near $x = 1.0$. The T_c for several representative MBE-grown cubic $\delta\text{-NbN}_x/\text{SiC}$ epitaxial films is shown in **Figure 10** along with representative published data for sputtered cubic $\delta\text{-NbN}_x$ films.^[55] The T_c of 16.7 K for the 50-nm-thick MBE-grown film is higher than the published results and indicates that improvements in the T_c of thinner MBE-grown films can be expected with further optimization of the MBE growth conditions. There is a common fall-off in T_c with decreasing thickness for very thin films. Modeling by Kang et al. indicates that the fall-off in T_c is best described by an electron wave leakage model (red line in the figure).^[55]

Other important superconducting properties include the mean-free-path, coherence length, residual resistivity ratio, electron density and mobility, and the magnetic properties of the materials. **Table 1** gives a brief summary of some of these properties for two MBE-grown cubic $\delta\text{-NbN}_x/\text{SiC}$ epitaxial films.^[56] Note that even at 5 nm thickness, the T_c of 6.41 K is substantially above the liquid helium temperature of 4.2 K. Also note that the coherence length of ≈ 10 nm in these two films is approximately double that of the typically cited value for cubic $\delta\text{-NbN}_x$.^[57] It is

Table 1. Selected properties of MBE-grown TMN superconductors.^[56]

	Symbol	5 nm NbN_x	35 nm NbN_x
Sheet resistance (Ω/\square)	R_{sh}	107.9	9.8
Carrier concentration (10^{23} cm^{-3})	n_{3D}	2.1	2.3
Electron Hall mobility ($\text{cm}^2 \text{Vs}^{-1}$)	μ	0.54	0.93
Mean free path (\AA)	l_{MFP}	6.6	11.6
Residual resistivity ratio	RRR	1.50	1.86
T_c (Resistance)	T_c	6.41	9.26
T_c (Magnetometry)	T_c	6.23	9.36
Coherence length (nm)	ξ	10.56	10.06
$[\text{N}]/[\text{Nb}]$	x	0.88	0.75

clear that MBE can be used to grow high-quality epitaxial superconducting NbN_x . A more detailed discussion of these parameters and the magnetic properties of these MBE-grown films is presented by Yan et al.^[56]

Hexagonal TaN_x has been reported for decades to be either non-superconducting or to have a T_c below 1.5 K.^[58] **Figure 11** shows the measured T_c for the MBE-grown 43-nm-thick epitaxial hexagonal TaN_x film is ≈ 1.25 K. Although this T_c is too low for many superconducting device applications, being below the liquid He temperature, there are applications such as superconductor/normal-metal/superconductor (S–N–S) Josephson junction devices where high-quality epitaxy of the entire structure would be appealing and $\text{NbN}_x/\text{Ta}_2\text{N}/\text{NbN}_x$ or other TaN_x -based structures may find applicability. For example, the AC Josephson effect using S–N–S junctions has been proposed as a programmable voltage standard.^[59]

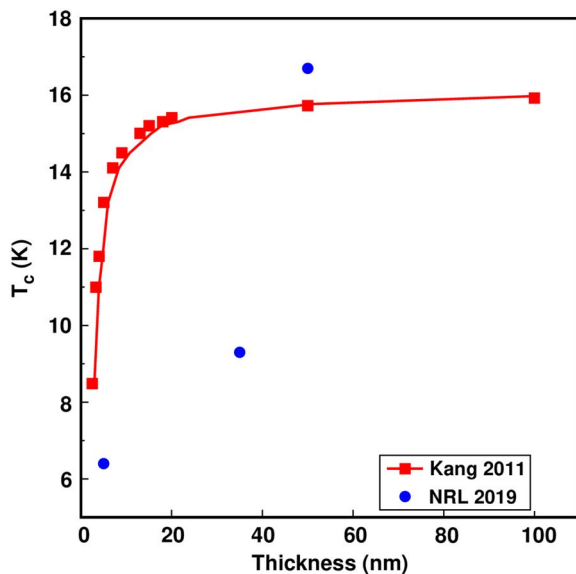


Figure 10. Measured superconducting transition temperature for three MBE-grown NbN_x films on SiC compared to measurements and modeling by Kang.^[55] The 50-nm-thick MBE-grown NbN_x layer T_c is 16.7 K and indicates the high quality of the film. Kang’s results indicate that further improvements in the T_c of thinner MBE-grown layers can be expected with further growth optimization.

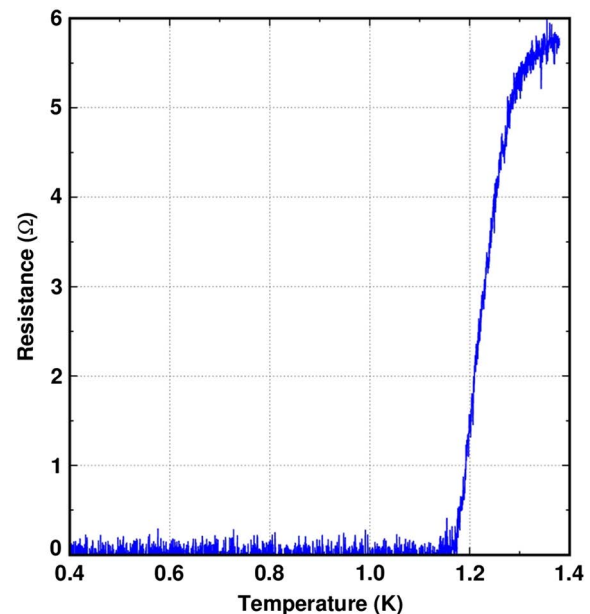


Figure 11. Measured superconducting transition temperature for 43-nm-thick TaN_x layer grown by MBE on 6H-SiC. The $T_c = 1.25$ K. This is the first reported measurement of the T_c of hexagonal TaN_x .

4. III-N Semiconductor/Superconductor Epitaxial Heterostructures on SiC

Although the lattice-mismatch between $\text{NbN}_x/\text{TaN}_x$ and III-N semiconductors materials can be larger than that to SiC, it is still possible to grow high-quality epitaxial III-N heterostructures on the TMNs. Integration of epitaxial buried superconducting ground planes with III-N devices could ease fabrication of low-loss microwave transmission lines and serve as a prototype for ground planes for Josephson junction arrays that are being contemplated as practical voltage standards.^[60] In addition, the different chemistry of TMNs compared with III-N semiconductors enables the possibility of strongly selective etching and epitaxial lift-off and transfer of III-N devices from the host substrate to other substrates that may offer better thermal conductivity or opportunities for heterogenous device integration.^[61] However, the hexagonal III-N materials and the TMNs have different crystal structures as their space groups differ. In particular, III-N materials are polar (i.e., they lack inversion symmetry) so that the metal-polar and nitrogen-polar faces of the $+/-$ [0001]-oriented crystals are different. In contrast, the cubic and hexagonal phases of NbN_x and some hexagonal phases of TaN_x have inversion symmetry so the $+/-$ [111]-faces of the cubic phases are equivalent as are the $+/-$ [0001]-faces of the hexagonal phases. This means that

one must carefully consider the atomic alignment of the polar/nonpolar interfaces in heterostructures comprised of III-N semiconductors and TMNs.

Figure 12 shows a simple ball-and-stick model of interfaces between TMNs and the III-N semiconductors of interest. It is well known that the cohesive energy increases rapidly as the interatomic distance decreases from the equilibrium value.^[62] As such, we expect (to first order) that SiC and III-N materials have closer-to-equilibrium atomic stacking on TMNs (as indicated by the blue arrow) when the epitaxial interface is grown N-polar up than when it is grown III-polar up (indicated by the red arrow). In other words, there is less bond distortion and lower cohesive energy when the cation separation across the interface is similar to the bulk value. Similarly, TMNs have closer-to-equilibrium atomic stacking on Si-face or III-polar material than on C-polar or N-polar material. (To date, attempts at MBE growth of high-quality TMNs on C-polar SiC have been unsuccessful.) This interfacial stacking model applies whether the TMN is the [111]-oriented cubic phase or the [0001]-oriented hexagonal phases. The polarity of the III-N semiconductor on the TMN can be changed to metal-polar in the usual way through the use of carefully tailored nucleation layers.^[63,64]

Another complication in the formation of heteroepitaxial junctions between TMNs and III-Ns is that the cubic [111]-oriented

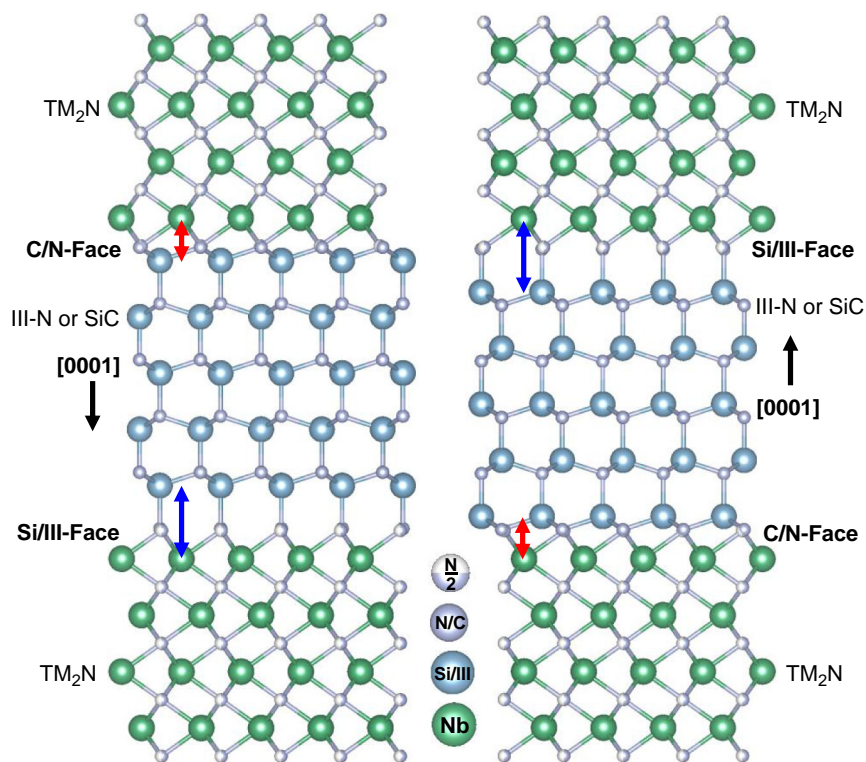


Figure 12. Ball-and-stick models of epitaxial heterostructures of III-N / SiC materials and TM_2N materials (e.g., Nb_2N or Ta_2N). As the III-N and SiC materials are polar, the (0001) and (000-1) surfaces are not equivalent. The blue arrows indicate interfacial stacking that would be favorable because the cation separation change is small on crossing the interface, whereas the red arrows indicate interfacial stacking that would be unfavorable because the cation atoms would be unnaturally close across the interface. This simple model indicates that TMNs prefer to grow on Si-face or III-face materials, whereas III-Ns prefer to grow N-polar up on TMNs.

TMNs can suffer from rotational twins and consequent formation of incoherent grain boundaries. Also, as Sands et al. point out, any differences in symmetry between heterojunction materials will, in general, lead to the formation of extended defects in the lower-symmetry material.^[2] These grain boundaries can lead to the formation of threading dislocations and other extended defects that can adversely impact electronic and optical devices made from these materials. Although it has not been a focus of this work, it is expected that twinning in the cubic TMNs can be reduced or eliminated by using the same types of optimizations as used for the growth of twin-free 3C-SiC on 4H-SiC (namely through control of the surface step density and orientation, and/or control of the surface chemistry and film nucleation).^[65,66]

High-quality epitaxial AlN layers have been grown in situ by MBE on NbN_x and TaN_x and have properties similar to those grown directly on SiC.^[67,68] For example, **Figure 13** shows the symmetric XRD data measured for a 200-nm-thick AlN/100-nm-thick δ-NbN_x/6H-SiC heterostructure grown by MBE. The peaks are sharp and in the expected positions for the [111]-oriented δ-NbN_x and hexagonal AlN phases. This result indicates that the high quality of the δ-NbN_x is preserved even after AlN overgrowth, and that high-quality AlN can be grown epitaxially on [111]-oriented δ-NbN_x.

Figure 14 shows a representative XTEM micrograph of a similar AlN/30-nm-thick δ-NbN_x/6H-SiC sample.^[67] The δ-NbN_x/SiC interface is sharp as is the AlN/δ-NbN_x interface. Unfortunately, the resolution in this particular image was too low to perform FFTs to verify the δ-NbN_x crystalline phase.

Electrical measurements of metal/AlN/δ-NbN_x/SiC capacitors showed that the epitaxial AlN on δ-NbN_x is of high electrical

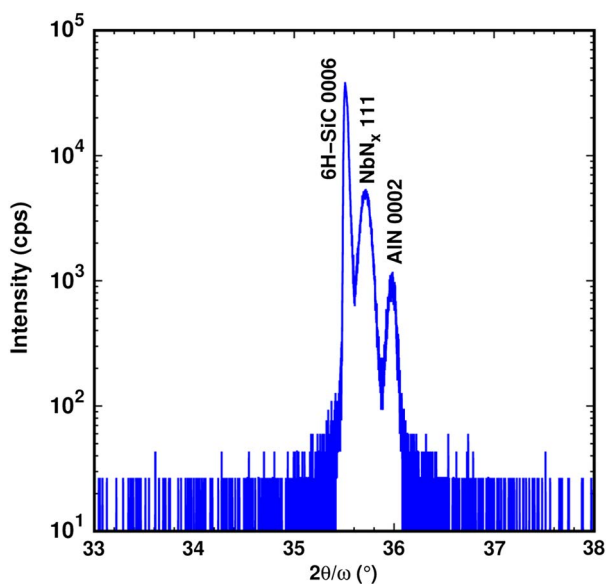


Figure 13. Symmetric XRD data measured on an MBE-grown 200 nm AlN/100 nm NbN_x/6H-SiC sample. The peaks are sharp and in the expected positions, indicating that high-quality AlN can be grown on NbN_x and that NbN_x is not degraded by the AlN overgrowth. Reproduced with permission.^[67] Copyright 2015, IOP Publishing.

quality as well.^[68] Vertical breakdown fields exceeding 5.5 MV cm⁻¹ were measured on simple MIM devices without any contact-edge termination optimizations.

Thick GaN layers can also be grown on TMNs with the expected properties. **Figure 15** shows a summary of a growth experiment in which GaN was grown by MBE for 24 h on AlN/NbN_x to see the effect of long temperature exposure and overgrowth on the 54-nm-thick MBE-grown NbN_x film and to measure the GaN properties.^[63] In this case, the GaN is Ga-polar as the polarity was flipped from N-polar to Ga-polar by growing a low-temperature (LT) AlN layer on the NbN_x film before growing the GaN. Post-growth AFM images show that the film is very smooth, with atomic-step terraces and an rms roughness of 0.24 nm. The XRD data shows Pendellösung fringes from the sharp NbN_x/SiC interface, and an intense and sharp GaN peak. The FWHM of the XRD rocking curve of the 0002 GaN peak is 45 arc-sec (not shown). Fitting of the optical reflectance oscillations shows the expected GaN bandgap feature and gives the expected growth rate. Although we expect stress in the GaN layer as a consequence of the thermal expansion mismatch between the GaN and the AlN/NbN_x/SiC layer stack, these results show that the stress is manageable (only low levels of cracking were seen via optical microscopy) even for thick GaN layers. This experiment shows that NbN_x tolerates long-duration high-temperature MBE growth cycles and that high-quality Ga-polar GaN can be grown epitaxially on NbN_x.

Finally, N-polar and Ga-polar high electron mobility transistor (HEMT) layers can be grown on epitaxial TMNs by MBE and achieve electrical quality comparable with those structures grown directly on SiC. **Figure 16a** shows a summary of N-polar GaN/AlGaN HEMTs grown on NbN_x.^[61] The structure includes a 30-nm-thick NbN_x layer, a 100-nm-thick AlN layer, and a 1.3-μm-thick GaN buffer, followed by a 30-nm-thick Al_{0.4}GaN barrier and a 30-nm-thick GaN channel. A representative dark-field cross-sectional scanning transmission electron micrograph (STEM) of the layers shows the abrupt interfaces and the usual reduction of the threading dislocation density in

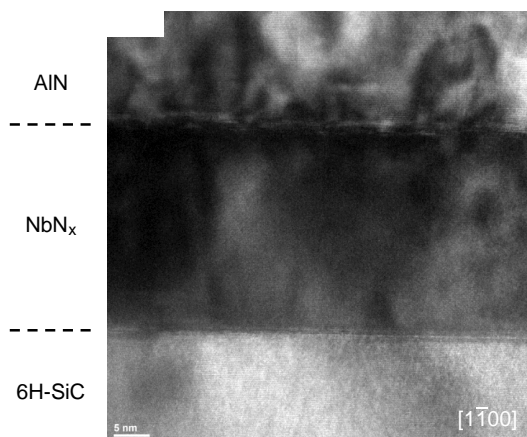


Figure 14. Cross-sectional transmission electron micrograph of an AlN/30 nm NbN_x/6H-SiC sample. The NbN_x/SiC interface is sharp, as is the AlN on NbN_x interface, indicating no intermixing between the materials. Reproduced with permission.^[67] Copyright 2015, IOP Publishing.

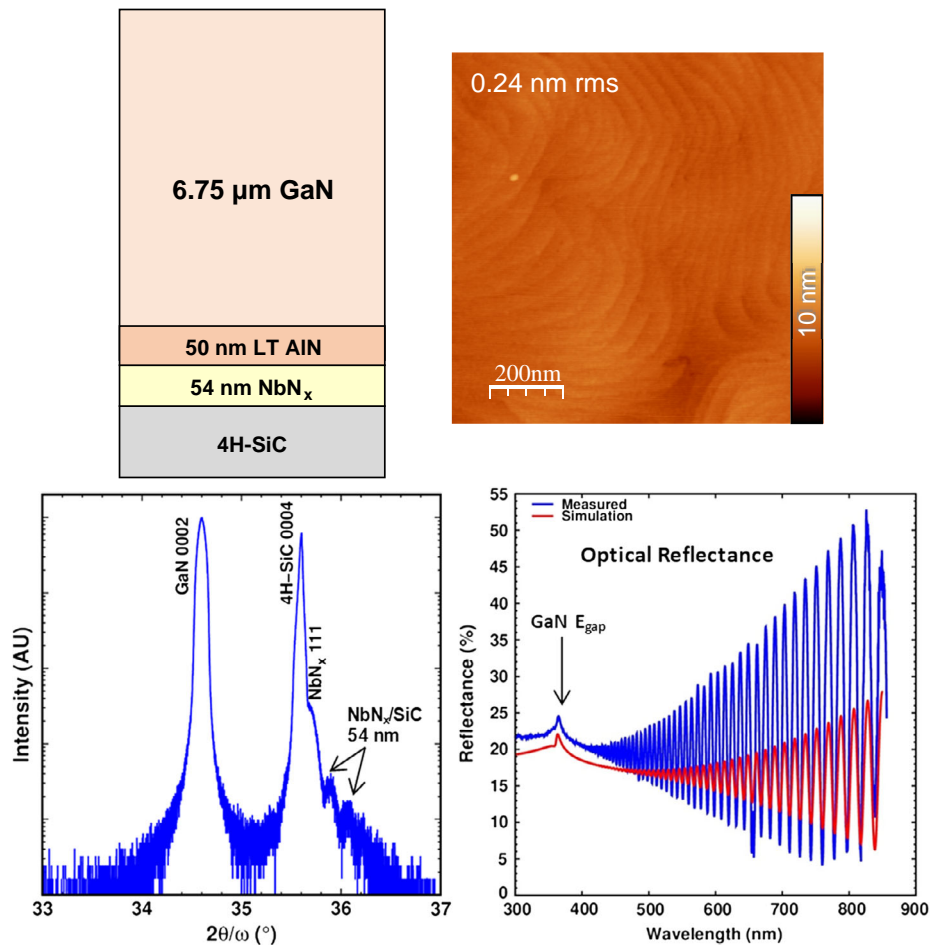


Figure 15. Summary of measurements of a 6.75 μm thick Ga-polar GaN layer grown on LT AlN on 54-nm-thick NbN_x /4H-SiC. The film has very low surface roughness and shows the atomic steps and high smoothness expected for high-quality Ga-polar material. The XRD data shows Pendellösung fringes, indicating a high-quality interface between the NbN_x layer and the SiC substrate. Optical reflectance measurements show that the GaN optical bandgap has the expected value and that the film thickness matches expectations.

the GaN as the layer thickness increases. The XRD indicates the layers are all present with high quality, and this is reflected in the DC characteristics of the fabricated HEMTs. The Hall effect mobility is $1375 \text{ cm}^2 \text{ V}^{-1} \text{ s}^{-1}$ with the channel density of $1.18 \times 10^{13} \text{ cm}^{-3}$, and both of these values are comparable to those obtained for a similar HEMT structure grown directly on SiC. The HEMT open-channel current exceeds 1 A mm^{-1} , and good pinch-off is obtained. In addition, breakdown to the buried NbN_x is not observed until the drain voltage exceeds 90 V ($\approx 7 \times 10^5 \text{ V cm}^{-1}$). Figure 16b shows an early Ga-polar HEMT structure consisting of a 45-nm-thick LT AlN layer on a 50-nm-thick NbN_x layer. The structure then includes a 1.2- μm -thick GaN buffer layer and a 25-nm-thick $\text{Al}_{0.28}\text{GaN}$ barrier. Although the XRD indicates the layers are of high quality, the carrier mobility is low at $995 \text{ cm}^2 \text{ V}^{-1} \text{ s}^{-1}$, thereby limiting the transistor current and performance. Further optimization of the Ga-polar GaN growth on TMNs is expected to result in higher channel transport performance that matches or exceeds the aforementioned N-polar results.

The N-polar HEMTs on NbN_x discussed earlier were recently studied at low temperature and at high magnetic fields to learn more about their electronic and magnetic properties.^[56] Most of the measurements were made using a Quantum Design PPMS system. As part of that work, electrical contact was created between the N-polar HEMT source and the buried NbN_x layer to use the NbN_x as an electrical load. As seen in Figure 17, the circuit functions as expected. The HEMT has good operating characteristics at low temperature, and as the temperature is swept through the T_c of this NbN_x film (7.7 K), the NbN_x changes from a normal conductor to a superconductor. When operated at 5 K, as the dissipated electrical power in the device increases and raises the NbN_x temperature above T_c , the I - V characteristics show a negative differential resistance when the metal changes from a superconductor to a normal metal. This is the first time such a phase change has been observed in epitaxial III-N/superconductor structures, and this indicates the promise of epitaxial integration of TMNs with III-N transistors for novel superconducting device and circuit applications.

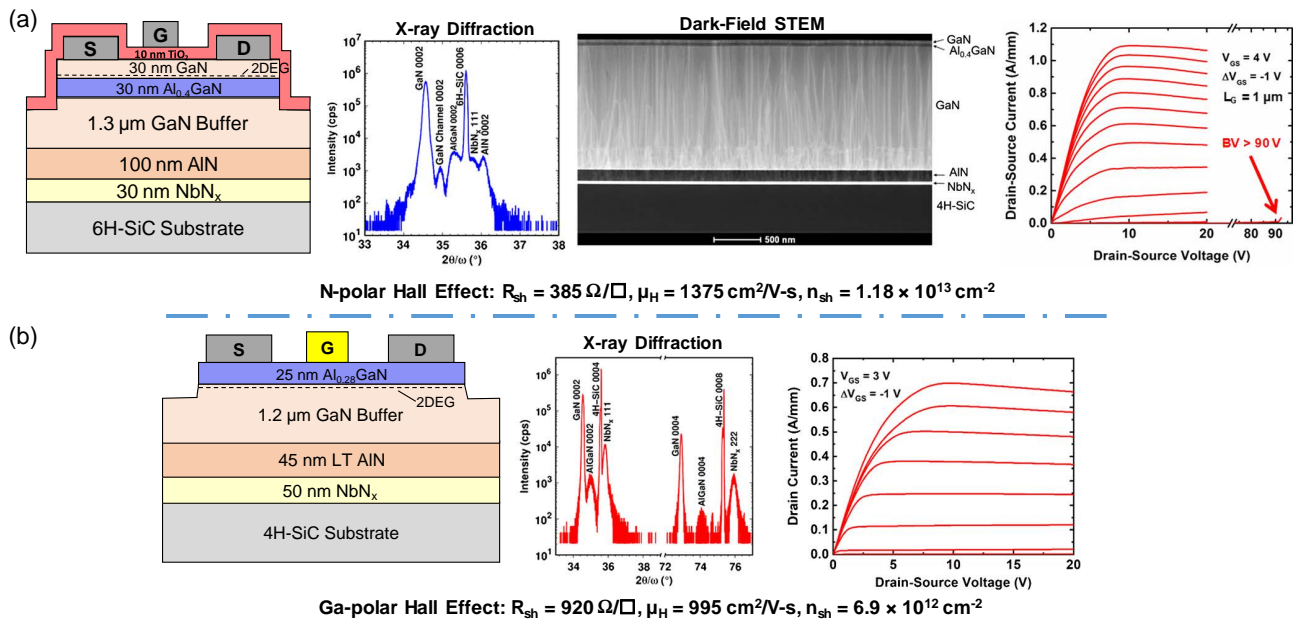


Figure 16. a) Summary of N-polar HEMT results obtained for the indicated structure grown on 30 nm NbN_x. Note the high quality of the X-ray data, the sharp interfaces and typical dislocation filtering with increasing thickness in the STEM image, and the high quality of the DC *I*-*V* drain characteristics. The Hall effect mobility was 1375 cm² Vs⁻¹ at a sheet density of 1.18 × 10¹³ cm⁻². These results are equivalent to those obtained for the same structure (without NbN_x) grown directly on SiC. Reproduced with permission.^[61] Copyright 2016, IEEE. b) Summary of early Ga-polar HEMT results obtained for the indicated structure grown on 50 nm NbN_x. The Ga-polar GaN polarity was obtained through the use of the 45 nm LT AlN layer. Although the X-ray data shows high quality, the low Hall effect mobility of 995 cm² Vs⁻¹ limits the device performance. Higher performance is expected upon improving the quality of the Ga-polar GaN growth on NbN_x.

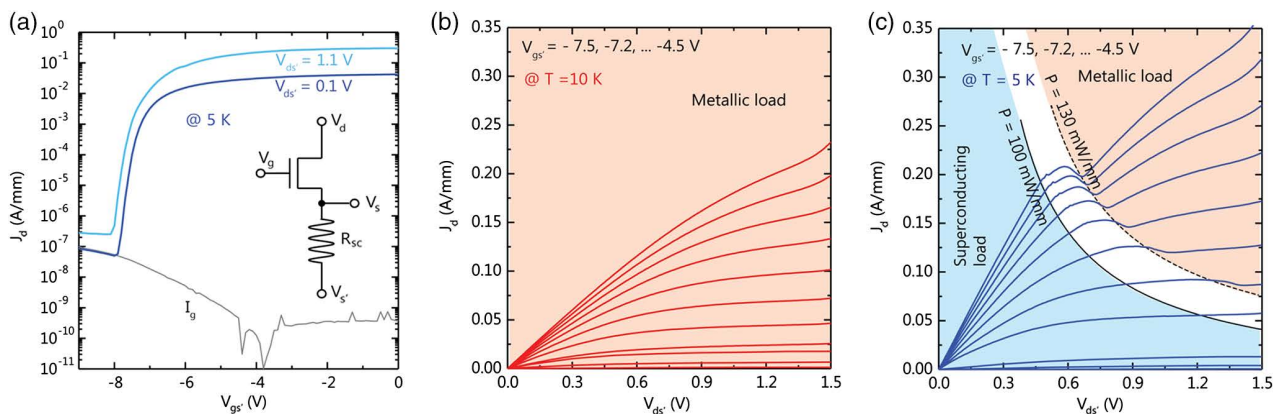


Figure 17. Summary of electrical measurements of MBE-grown N-polar HEMT on NbN_x using the NbN_x as a superconducting electrical load. a) Transfer characteristics and inset electrical circuit diagram. b) Drain *I*-*V* characteristics at 10 K, above the 7.7 K *T*_c of the NbN_x layer. c) Drain *I*-*V* characteristics at 5 K showing two regions of operation depending on whether the NbN_x layer is superconducting (low-power region) or a normal metal (high-power region). A region of negative differential resistance is present between the low and high-power region. Reproduced with permission.^[56] Copyright 2018, Springer Nature.

5. Conclusion

The benefits of the epitaxial integration of cubic δ-NbN_x, hexagonal β-Nb₂N, and hexagonal TaN_x with SiC and group III nitride semiconductors have been discussed. These materials are nearly lattice-matched and can be grown by MBE to yield

high-quality films as shown by a variety of characterization techniques. Direct epitaxy of III-N semiconductor materials, including GaN HEMTs, has been demonstrated on superconducting cubic δ-NbN_x, and the device characteristics show the promise of this unique epitaxial semiconductor–superconductor materials system.

Acknowledgements

This work was supported by the Office of Naval Research (Dr. Paul Maki), with additional support at Cornell from the National Science Foundation. The authors appreciate the use of L.B. Ruppalt's Lake Shore Cryotronics probe station for some of the T_c measurements at NRL.

Conflict of Interest

The authors declare no conflict of interest.

Keywords

molecular beam epitaxy, superconductors, transition metal nitrides, transmission electron diffraction, x-ray diffraction

Received: August 19, 2019

Revised: October 2, 2019

Published online: November 11, 2019

- [1] S. M. Sze, H. K. Gummel, *Solid-State Electron.* **1966**, *9*, 751.
- [2] T. Sands, C. J. Palmström, J. P. Harbison, V. G. Keramidas, N. Tabatabaie, T. L. Cheeks, R. Ramesh, Y. Silverberg, *Mater. Sci. Rep.* **1990**, *5*, 99.
- [3] N. L. Okamoto, M. Kusakari, K. Tanaka, H. Inui, M. Yamaguchi, S. Otani, *Jpn. Appl. Phys.* **2003**, *42*, 88.
- [4] R. Armitage, J. Suda, T. Kimoto, in *Nitride and Wide Bandgap Semiconductors for Sensors, Photonics, and Electronics V* (Eds: H. M. Ng, A. G. Baca), Electrochemical Society Proc., Vol. 2004-06, Pennington, NJ, USA **2004**, pp. 484–495.
- [5] K. Manandhar, M. Rashidi-Alavijeh, M. Trenary, P. Zapol, in *Abstracts of Papers of the American Chemical Society*, Vol. 246, American Chemical Society, Washington, DC **2013**.
- [6] J. A. Freitas Jr., L. B. Rowland, J. Kim, M. Fatemi, *Appl. Phys. Lett.* **2007**, *90*, 091910.
- [7] S. I. Maximenko, J. A. Freitas Jr., J. A. Mittereder, L. B. Rowland, J. Kim, *Appl. Phys. Lett.* **2008**, *92*, 212104.
- [8] S. Krause, D. Meledin, V. Desmaris, A. Pavolotsky, V. Belitsky, M. Rudzinski, E. Pippel, *Supercond. Sci. Technol.* **2014**, *27*, 065009.
- [9] D. Sam-Giao, S. Pouget, C. Bougerol, E. Monroy, A. Grimm, S. Jebari, M. Hofheinz, J.-M. Gerard, V. Zwiller, *AIP Adv.* **2014**, *4*, 107123.
- [10] L. E. Toth, *Transition Metal Carbides and Nitrides*, Academic Press, New York, USA **1971**, pp. 4–9.
- [11] B. Navinsek, S. Seal, *JOM* **2001**, *53*, 51.
- [12] W. H. P. Pernice, C. Schuck, O. Minaeva, M. Li, G. N. Goltsman, A. V. Sergienko, H. X. Tang, *Nat. Commun.* **2012**, *3*, 1325.
- [13] M. Faucher, T. Fournier, B. Pannetier, C. Thirion, W. Wernsdorfer, J. C. Villegier, V. Bouchiat, *Phys. C* **2002**, *368*, 211.
- [14] S. N. Song, B. Y. Jin, H. Q. Yang, J. B. Ketterson, I. K. Schuller, *Jpn. J. Appl. Phys.* **1987**, *26*, 1615.
- [15] G. N. Gol'tsman, O. Okunev, A. A. Chulkova, A. Semenov Lipatov, K. Smirnov, B. Voronov, A. Dzardanov, *Appl. Phys. Lett.* **2001**, *79*, 705.
- [16] M. Hajenius, J. J. A. Baselmans, J. R. Gao, T. M. Klapwijk, P. A. J. de Korte, B. Voronov, G. Gol'tsman, *Supercond. Sci. Technol.* **2004**, *17*, S224.
- [17] W. Pies, A. Weiss, in *Landolt–Börnstein: Group III Condensed Matter, Vol. 7c1* (Eds: K. H. Hellwege, A. M. Hellwege, Springer, Heidelberg **1978**, pp. 50, 55.
- [18] K. Momma, F. Izumi, *J. Appl. Crystallogr.* **2011**, *44*, 1272.
- [19] H. Romanus, G. Teichert, L. Spiess, *Mater. Sci. Forum* **1998**, *264–268*, 437.
- [20] R. W. G. Wyckoff, *Crystal Structures*, Vol. 1, Interscience Publishers, New York, USA **1963**, pp. 85–237.
- [21] D. Jena, R. Page, J. Casamento, P. Dang, J. Singhal, Z. Zhang, J. Wright, G. Khalsa, Y. Cho, H. G. Xing, *Jpn. J. Appl. Phys.* **2019**, *58*, SC0801.
- [22] Y. Yue, Z. Hu, J. Guo, B. Sensale-Rodriguez, G. Li, R. Wang, F. Faria, B. Song, X. Gao, S. Guo, *Jpn. J. Appl. Phys.* **2013**, *52*, 08JN14.
- [23] W. Li, S. Sharmin, H. Ilatikhameneh, R. Rahman, Y. Lu, J. Wang, X. Yan, A. Seabaugh, G. Klimeck, D. Jena, P. Fay, *IEEE J. Exp. Solid State Comput. Devices Circuits* **2015**, *1*, 28.
- [24] Z. Hu, K. Nomoto, B. Song, M. Zhu, M. Qi, M. Pan, X. Gao, V. Protasenko, D. Jena, H. G. Xing, *Appl. Phys. Lett.* **2015**, *107*, 243501.
- [25] S. M. Islam, K. Lee, J. Verma, V. Protasenko, S. Rouvimov, S. Bharadwaj, H. G. Xing, D. Jena, *Appl. Phys. Lett.* **2017**, *110*, 041108.
- [26] J. K. Sheu, S. J. Chang, C. H. Kuo, Y. K. Su, L. W. Wu, Y. C. Lin, W. C. Lai, J. M. Tsai, G. C. Chi, R. K. Wu, *IEEE Photonics Technol. Lett.* **2003**, *15*, 18.
- [27] M.-A. Dubois, C. Muller in *MEMS-based Circuits and Systems for Wireless Communication* (Eds: C. C. Enz, A. Kaiser), Springer, New York **2013**, pp. 3–28.
- [28] V. Mourik, K. Zuo, S. M. Frolov, S. R. Plissard, E. P. A. M. Bakkers, L. P. Kouwenhoven, *Science* **2012**, *336*, 1003.
- [29] S. D. Sarma, M. Freedman, C. Nayak, *npj Quant. Inf.* **2015**, *1*, 15001.
- [30] P. Krogstrup, N. L. B. Ziiino, W. Chang, S. M. Albrecht, M. H. Madsen, E. Johnson, J. Nygård, C. M. Marcus, T. S. Jespersen, *Nat. Mater.* **2015**, *14*, 400.
- [31] D. J. Meyer, B. P. Downey, D. S. Katzer (U. S. Navy), USA 10,340,353 B2, **2019**.
- [32] H.-M. Zhang, Y. Sun, W. Li, J.-P. Peng, C.-L. Song, Y. Xing, Q. Zhang, J. Guan, Z. Li, Y. Zhao, S. Ji, L. Wang, K. He, X. Chen, L. Gu, L. Ling, M. Tian, L. Li, X. C. Xie, J. Liu, H. Yang, Q.-K. Xue, J. Wang, X. Ma, *Phys. Rev. Lett.* **2015**, *114*, 107003.
- [33] Y. Xing, H.-M. Zhang, H.-L. Fu, H. Liu, Y. Sun, J.-P. Peng, F. Wang, X. Lin, X.-C. Ma, Q.-K. Xue, J. Wang, X. C. Xie, *Science* **2015**, *350*, 542.
- [34] V. Kochat, A. Samanta, Y. Zhang, S. Bhowmick, P. Manimunda, S. A. S. Asif, A. S. Stender, R. Vajtai, A. K. Singh, C. S. Tiwary, P. M. Ajayan, *Sci. Adv.* **2018**, *4*, e1701373.
- [35] D. S. Katzer, D. J. Meyer, D. F. Storm, N. Nepal, V. D. Wheeler, *J. Vac. Sci. Technol. B* **2014**, *32*, 02C117.
- [36] D. S. Katzer, D. J. Meyer, D. F. Storm, J. A. Mittereder, V. M. Bermudez, S. F. Cheng, G. G. Jernigan, S. C. Binari, *J. Vac. Sci. Technol. B* **2012**, *30*, 02B129.
- [37] T. H. Myers, M. R. Millecchia, A. J. Ptak, K. S. Ziemer, C. D. Stinespring, *J. Vac. Sci. Technol. B* **1999**, *17*, 1654.
- [38] E. K. Storms, *Special Report to the Phase Equilibria Program*, American Ceramic Society, Westerville, OH **1989**, https://phaseonline.ceramics.org/ped_figure_search (accessed: April 2016).
- [39] D. S. Katzer, N. Nepal, D. J. Meyer, B. P. Downey, V. D. Wheeler, D. F. Storm, M. T. Hardy, *Appl. Phys. Express* **2015**, *8*, 085501.
- [40] D. S. Katzer, N. Nepal, M. T. Hardy, B. P. Downey, D. F. Storm, E. N. Jin, D. J. Meyer, *J. Vac. Sci. Technol. B* **2019**, *37*, 031211.
- [41] B. V. Shanabrook, J. R. Waterman, J. L. Davis, R. J. Wagner, *Appl. Phys. Lett.* **1992**, *61*, 2338.
- [42] B. Heying, R. Averbeck, L. F. Chen, E. Haus, H. Riechert, J. S. Speck, *J. Appl. Phys.* **2000**, *88*, 1855.
- [43] G. Y. Wang, Z. Zhu, X. Y. Yang, L. Dong, H. Y. Ma, H. H. Sun, A. M. Li, D. D. Guan, D. Qian, C. Liu, Y. Y. Li, J. F. Jia, *APL Mater.* **2017**, *5*, 126107.
- [44] I. Stoica, E. G. Hitruc, D. Timpu, V. Barboiu, D. S. Vasilescu, *Scanning* **2015**, *37*, 355.
- [45] G. L. Miller, D. A. H. Robinson, J. D. Wiley, *Rev. Sci. Instrum.* **1976**, *47*, 799.

- [46] R. Sanjinés, M. Benkahoul, C. S. Sandu, P. E. Schmid, F. Lévy, *Thin Solid Films* **2006**, 494, 190.
- [47] G. R. Witt, *Thin Solid Films* **1972**, 13, 109.
- [48] A. H. Farah, A. O. Er, Y. Ufuktepe, G. Myneni, H. E. Elsayed-Ali, *Appl. Surf. Sci.* **2011**, 258, 1613.
- [49] M. Benkahoul, *Doctor of Sciences*, École Polytechnique Fédérale de Lausanne **2005**.
- [50] V. G. Brauer, R. Esselborn, *Z. Anorg. Allg. Chem.* **1961**, 309, 151.
- [51] A. R. Kramer, J. E. Yater, unpublished.
- [52] R. Sanjinés, M. Benkahoul, M. Papagano, F. Lévy, *J. Appl. Phys.* **2006**, 99, 044911.
- [53] K. W. Andrews, D. J. Dyson, S. R. Keown, *Interpretation of Electron Diffraction Patterns*, Hilger and Watts, London, UK **1967**, p. 128.
- [54] CrystalMaker Software Ltd, Oxford, England, www.crystallmaker.com (accessed: June 2017).
- [55] L. Kang, B. B. Jin, X. Y. Liu, X. Q. Jia, J. Chen, Z. M. Ji, W. W. Xu, P. H. Wu, S. B. Mi, Y. J. Wu, B. G. Wang, *J. Appl. Phys.* **2011**, 109, 033908.
- [56] R. Yan, G. Khalsa, S. Vishwanath, Y. Han, J. Wright, S. Rouvimov, D. S. Katzer, N. Nepal, B. P. Downey, D. A. Muller, H. G. Xing, D. J. Meyer, D. Jena, *Nature* **2018**, 555, 183.
- [57] A. V. Narlikar, *The Oxford Handbook of Small Superconductors*, Oxford University Press, Oxford, UK **2017**, p. 6.
- [58] D. Gerstenberg, P. M. Hall, *J. Electrochem. Soc.* **1964**, 111, 936.
- [59] S. P. Benz, *Appl. Phys. Lett.* **1995**, 67, 2714.
- [60] C. A. Hamilton, *Rev. Sci. Instrum.* **2000**, 71, 3611.
- [61] D. J. Meyer, B. P. Downey, D. S. Katzer, N. Nepal, V. D. Wheeler, M. T. Hardy, T. J. Anderson, D. F. Storm, *IEEE Trans. Semicond. Manuf.* **2016**, 29, 384.
- [62] L. M. Hale, Z. T. Trautt, C. A. Becker, *Modell. Simul. Mater. Sci. Eng.* **2018**, 25, 055003.
- [63] D. S. Katzer, presented at North Am. Conf. on Molecular Beam Epitaxy (NAMBE 32), Saratoga Springs, NY, USA, September, **2016**.
- [64] M. D. Brubaker, S. M. Duff, T. E. Harvey, P. T. Blanchard, A. Roshko, A. W. Sanders, N. A. Sanford, K. A. Bertness, *Cryst. Growth Des.* **2015**, 16, 596.
- [65] L. Latu-Romain, D. Chaussende, M. Pons, *Cryst. Growth Des.* **2006**, 6, 2788.
- [66] K. Alassaad, M. Vivona, V. Soulière, B. Doisneau, F. Cauwet, D. Chaussende, F. Giannazzo, F. Roccaforte, G. Ferro, *ECS J. Solid State Sci. Technol.* **2014**, 3, P285.
- [67] N. Nepal, D. S. Katzer, D. J. Meyer, D. F. Storm, B. P. Downey, V. D. Wheeler, D. F. Storm, M. T. Hardy, *Appl. Phys. Express* **2016**, 9, 021003.
- [68] B. P. Downey, D. S. Katzer, N. Nepal, D. J. Meyer, D. F. Storm, V. D. Wheeler, M. T. Hardy, *Electron. Lett.* **2016**, 52, 1263.